Molecular Crystals and Liquid Crystals

ISSN: 1542-1406 (Print) 1563-5287 (Online) Journal homepage: http://www.tandfonline.com/loi/gmcl20

Co(II), Co(II)+Mn(II), Co(II)+Ni(II) Co-doping Effects on Tris(thiourea)zinc(II) Sulphate Crystals: A Comparative Study

M. Rajasekar, K. Meena, K. Muthu, G. Bhagavannarayana & SP. Meenakshisundaram

To cite this article: M. Rajasekar, K. Meena, K. Muthu, G. Bhagavannarayana & SP. Meenakshisundaram (2015) Co(II), Co(II)+Mn(II), Co(II)+Ni(II) Co-doping Effects on Tris(thiourea)zinc(II) Sulphate Crystals: A Comparative Study, Molecular Crystals and Liquid Crystals, 623:1, 179-193, DOI: 10.1080/15421406.2014.991146

To link to this article: http://dx.doi.org/10.1080/15421406.2014.991146

Mol. Cryst. Liq. Cryst., Vol. 623: pp. 179–193, 2015

ISSN: 1542-1406 print/1563-5287 online
DOI: 10.1080/15421406.2014.991146

Co(II), Co(II)+Mn(II), Co(II)+Ni(II) Co-doping Effects on Tris(thiourea)zinc(II) Sulphate Crystals: A Comparative Study

M. RAJASEKAR,[1] K. MEENA,[1] K. MUTHU,[1,2]
G. BHAGAVANNARAYANA,[3]
AND SP. MEENAKSHISUNDARAM[1,*]

[1]Department of Chemistry, Annamalai University, Annamalainagar, Tamil Nadu, India
[2]Centre for Research and Development, PRIST University, Vallam, Thanjavur, India
[3]Crystal Growth & X-ray Analysis Activity, CSIR- NPL, New Delhi, India

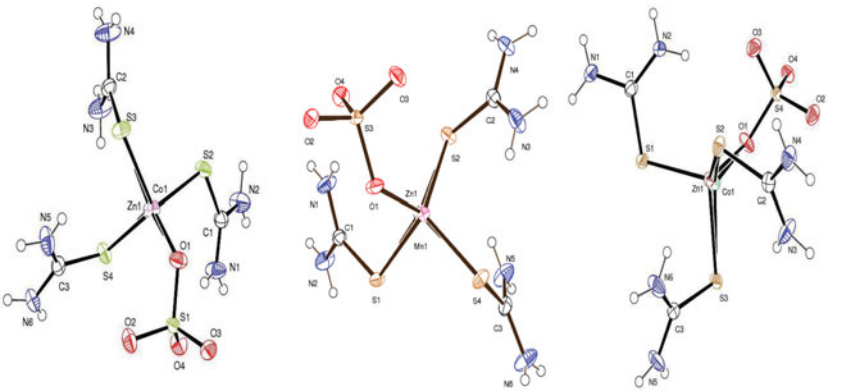

The influence of Co(II), Co(II)+Mn(II), Co(II)+Ni(II) co-doping on the structure and crystalline perfection of tris(thiourea)zinc(II) sulphate single crystals grown from an aqueous solution at room temperature by slow evaporation solution growth technique has been investigated. The incorporation of foreign metal into the crystalline lattice was well confirmed by chemical formula determined by single-crystal X-ray diffraction analysis. The intensity variations observed in powder X-ray diffraction patterns and slight shifts in vibrational frequencies in Fourier transform IR indicate the lattice stress. Thermal studies reveal the purity of the material and no decomposition is observed up to the melting point. High-resolution X-ray diffraction studies reveal that Co(II)-doped specimen has no clustering of defects while the Co(II)+Mn(II), Co(II)+Ni(II) co-doped crystals show the presence of structural grain boundaries as a result of crystal stress and strain. The as-grown crystals are further characterized by Kurtz powder technique and dielectric studies. Good transparency in the visible region is observed for all the

* Address correspondence to SP. Meenakshisundaram, Department of Chemistry, Annamalai University, Annamalainagar, Tamil Nadu 608 002, India. E-mail: aumats2009@gmail.com

Color versions of one or more of the figures in the article can be found online at www.tandfonline.com/gmcl.

specimens. Interestingly, in co-doping the host crystal selectively accommodates only one foreign metal ion as revealed by single-crystal XRD analysis.

Keywords Band gap energy; crystal growth; HRXRD; nonlinear optics; thermal analysis; X-ray diffraction

1. Introduction

Tris(thiourea)zinc(II) sulphate (ZTS) is a potential nonlinear optical (NLO) material which finds applications in the area of laser technology, optical communication, data storage technology, and optical computing because it has high resistance to laser induced damage, high nonlinearity, wide transparency, low angular sensitivity and good mechanical hardness compared to many organic NLO crystals [1–4]. Metal ion-doped materials are currently receiving a great deal of attention due to the rapid development of laser diodes [5,6]. The incorporation of transition metal into the host crystal will affect the growth process and physical properties.

Recently, we have investigated the Mn(II) doping effects on ZTS [7]. In the present investigation, we report the Co(II), Co(II)+Mn(II), and Co(II)+Ni(II) co-doping effects on ZTS. A comparative account is made for doped specimens characterized by XRD, HRXRD, FT-IR, TG/DTA, UV, SHG, and dielectric behavior.

2. Experimental

2.1. Synthesis and Crystal Growth

ZTS was synthesized as reported earlier [8]. Stoichiometric quantities of zinc sulphate heptahydrate (EM), cobalt sulphate heptahydrate (EM) and thiourea (SQ) were taken in the molar ratio 0.5:0.5:3. To avoid decomposition, low temperature ($<70^{\circ}$C) was maintained during the preparation of the solution in deionized water. After successive recrystallization, crystals were grown by slow evaporation solution growth technique. The crystallization took place within 15–20 days and the crystals were harvested.

Co-doping with Co(II) i.e. Mn(II) + Co(II) and Ni(II) + Co(II) were carried out using equimolar ratios. Photographs of as-grown pure and co-doped crystals are shown in Fig. 1.

2.2. Characterization Techniques

The structural analysis was carried out by using Bruker AXS (Kappa APEXII) X-ray diffractometer. Single-crystal XRD data were collected on a diffraction system that employs graphite monochromated Mo Kα_1 radiation ($\lambda = 0.71073$ Å). The structures were solved and refined by full matrix least squares on F^2 with WinGx software package utilizing SHELXS97 and SHELXL97 modules. All non-H atoms were refined anisotropically. Fourier transform infrared spectrum was recorded using AVATAR 330 FT-IR spectrometer. The powder XRD pattern is recorded by PANalytical X'pert PRO X-ray diffractometer with a graphite monochromated Cu Kα radiation at room temperature using a wavelength of 1.540 Å with a step size of 0.008°. UV-vis spectrum was recorded using CARY 5E UV-vis spectrophotometer. Thermogravimetric (TG) and differential thermal analysis (DTA) were carried out using a NETZSCH STA 449 F3 thermal analyzer in nitrogen atmosphere. Second harmonic generation (SHG) efficiency of the specimens were measured by the Kurtz powder technique [9]. Dielectric measurement of the crystals were carried out by the parallel plate capacitor method as a function of

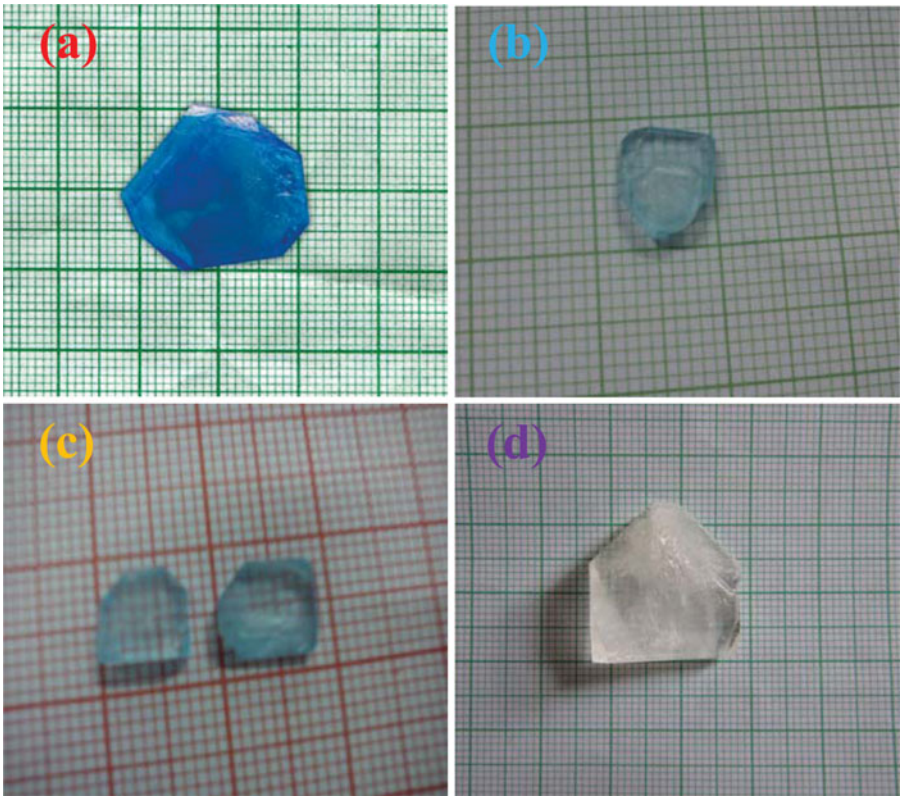

Figure 1. Photographs of as-grown (a) Co(II)-doped, (b) Co(II)+ Mn(II)-doped, (c) Co(II)+ Ni(II)-doped and (d) Pure ZTS Crystals.

temperature for various frequencies using a precision LCR meter (AGILENT 4284 A model).

To evaluate the crystalline perfection of the specimen crystals, high-resolution X-ray diffraction (HRXRD) analysis was carried out. A multicrystal X-ray diffractometer developed at National Physical Laboratory, New Delhi [10], was used to record high-resolution rocking or diffraction curves (DCs). In this system, a fine focus (0.4×8 mm^2; 2 kW Mo) X-ray source energized by a well-stabilized Philips X-ray generator (PW 1743) was employed. The well-collimated and monochromated Mo Kα_1 beam obtained from the three Si monochromator crystals set in dispersive $(+,-,-)$ configuration was used as the exploring X-ray beam. Before recording the diffraction curve, to remove the noncrystallized solute atoms remained on the surface of the crystal and also to ensure the surface planarity, the specimens were first lapped and chemically etched in a nonpreferential etchant of water and acetone mixture in 1:2 volume ratios. The diffracted intensity is measured by using a scintillation counter. The DCs were recorded by changing the glancing angle (the angle between the incident X-ray beam and the surface of the specimen) around the Bragg diffraction peak position θ_B (taken as zero as a reference point) starting from a suitable arbitrary glancing angle (θ). The detector was kept at the same angular position $2\theta_B$ with wide opening for its slit, the so-called ω scan [11].

Table 1. FT-IR frequencies (cm^{-1})

S. No.	Thiourea	Pure ZTS	Co(II)+ Ni (II)-doped ZTS	Co(II)+ Mn (II)-doped ZTS	Co(II)-doped ZTS	Assignment of vibrations
1	3376	3399	3386	3386	3386	$\nu_{as}(NH_2)$
2	3167	3195	3197	3197	3197	$\nu_{s}(NH_2)$
3	1627	1624	1627	1626	1626	$\delta(NH_2)$
4	1089	1122	1123	1125	1124	ν_{s}(C-N)
5	1472	1502	1508	1503	1506	ν(N-C-N)
6	1417	1398	1400	1400	1400	$\nu_{as}(C = S)$
7	740	712	714	714	714	$\nu_{s}(C = S)$
8	648	619	619	619	618	ν_{as}(N-C-S)

3. Results and Discussion

3.1. FT-IR

A close observation of FT-IR spectra of pure and doped specimens (Fig. 2) reveals that the metal incorporation results in small shifts in some of the characteristic vibrational frequencies are observed (Table 1). The minor structural changes resulting in disturbed vibrational patterns could be associated with stress as a result of dopant incorporation.

3.2. XRD

The indexed powder XRD patterns of all doped specimens are shown in Fig. 3. No new peaks or phases were observed by small quantity incorporation of metal ion. Anyway, intensity variations are observed. The most prominent peaks with maximum intensity of the XRD patterns of pure and co-crystallized specimens are quite different. These observations could be attributed to strains in the lattice.

The structural analysis was carried out by single-crystal XRD analysis. The ORTEP diagrams of all doped specimens are given in Fig. 4. All crystallize in the orthorhombic system with noncentrosymmetric space group $Pca2_1$ similar to ZTS. It is interesting to observe that the Co(II)+ Mn(II) co-doping results in the incorporation of small quantity Mn(II) in the host crystal while in Co(II)+Ni(II) co-doping the incorporation is preferential for Co(II). Other methods of chemical analysis would be able to detect the presence of less selective ions, may be at lower levels inaccessible for the used method. The ORTEP diagram show that both central metal atoms are surrounded by three sulphur atoms from three thiourea molecules and one oxygen atom from a sulphate group. The crystal data for all doped specimens are listed in Table 2. Fig. 4a reveals that the metal is coordinated by three thiourea groups with Zn/Co−S−C bond angles ranging from 101.65(12)° to 108.9(7)°, S−Zn/Co−S bond angles ranging from 102.71(17)° to 115.09(9)° and Zn/Co– S bond lengths lying in the range 2.25(4) Å to 2.39(3) Å in a distorted tetrahedral geometry. The Zn−S, Zn−O bond distances are slightly different from Co−S and Co−O bond distances. The S−Zn/Co−O bond angles range from 105.51(11)° to 114.4(2)° and Zn−S−Co bond angles fall in the range of 2.1 (7)° to 2.8(7)°.

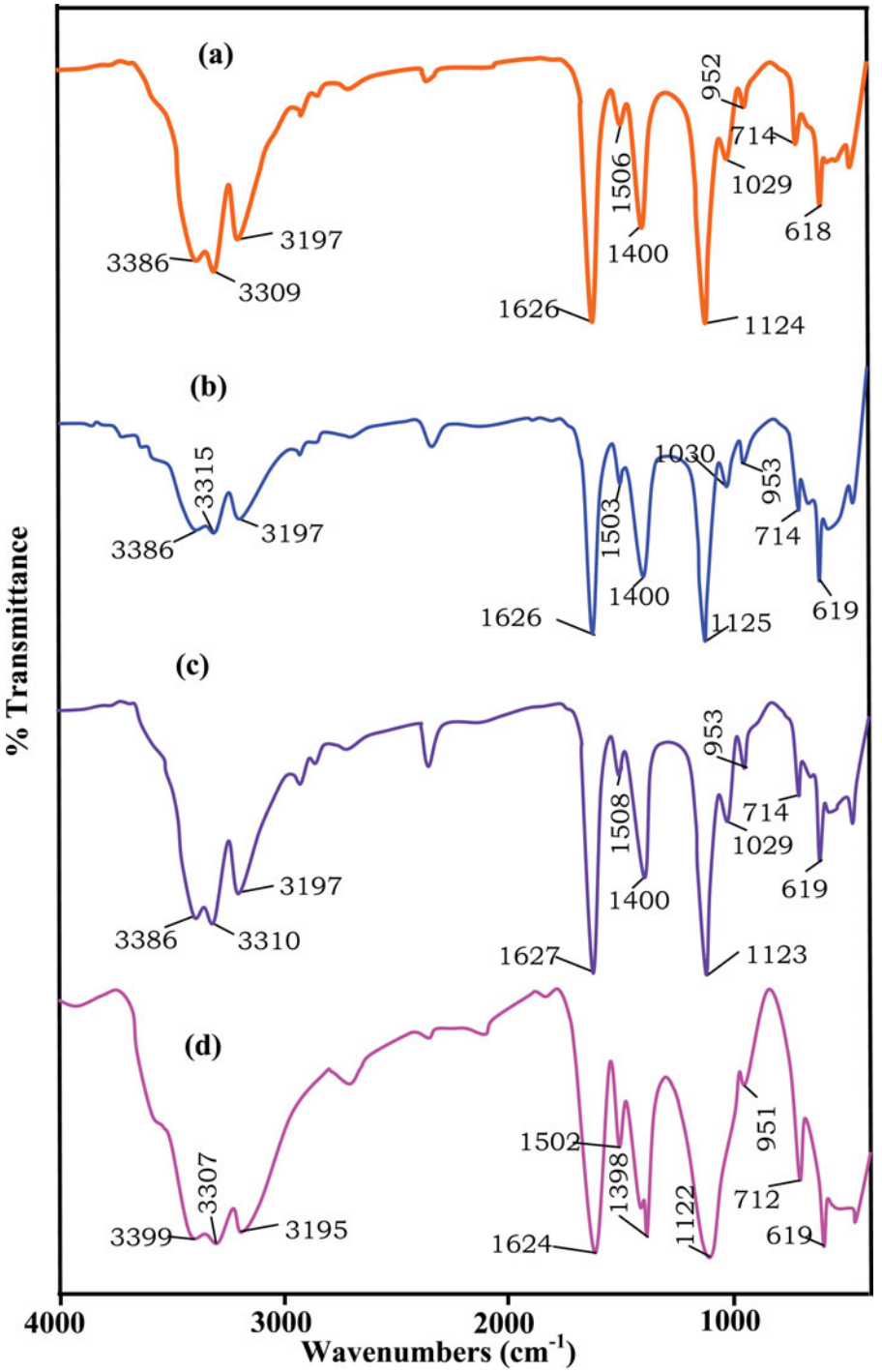

Figure 2. FT-IR spectra of (a) Co(II)-doped, (b) Co(II)+ Mn(II)-doped, (c) Co(II)+ Ni(II)-doped and (d) Pure ZTS Crystals.

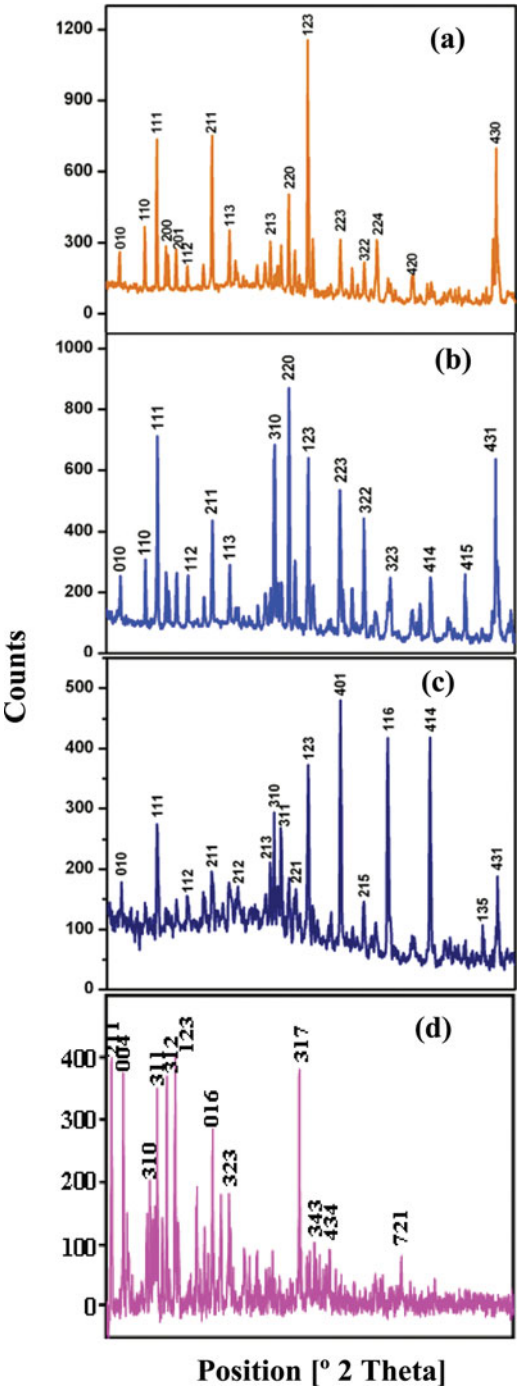

Figure 3. Powder XRD patterns of (a) Co(II)-doped, (b) Co(II)+ Mn(II)-doped, (c) Co(II)+ Ni(II)-doped and (d) Pure ZTS Crystals.

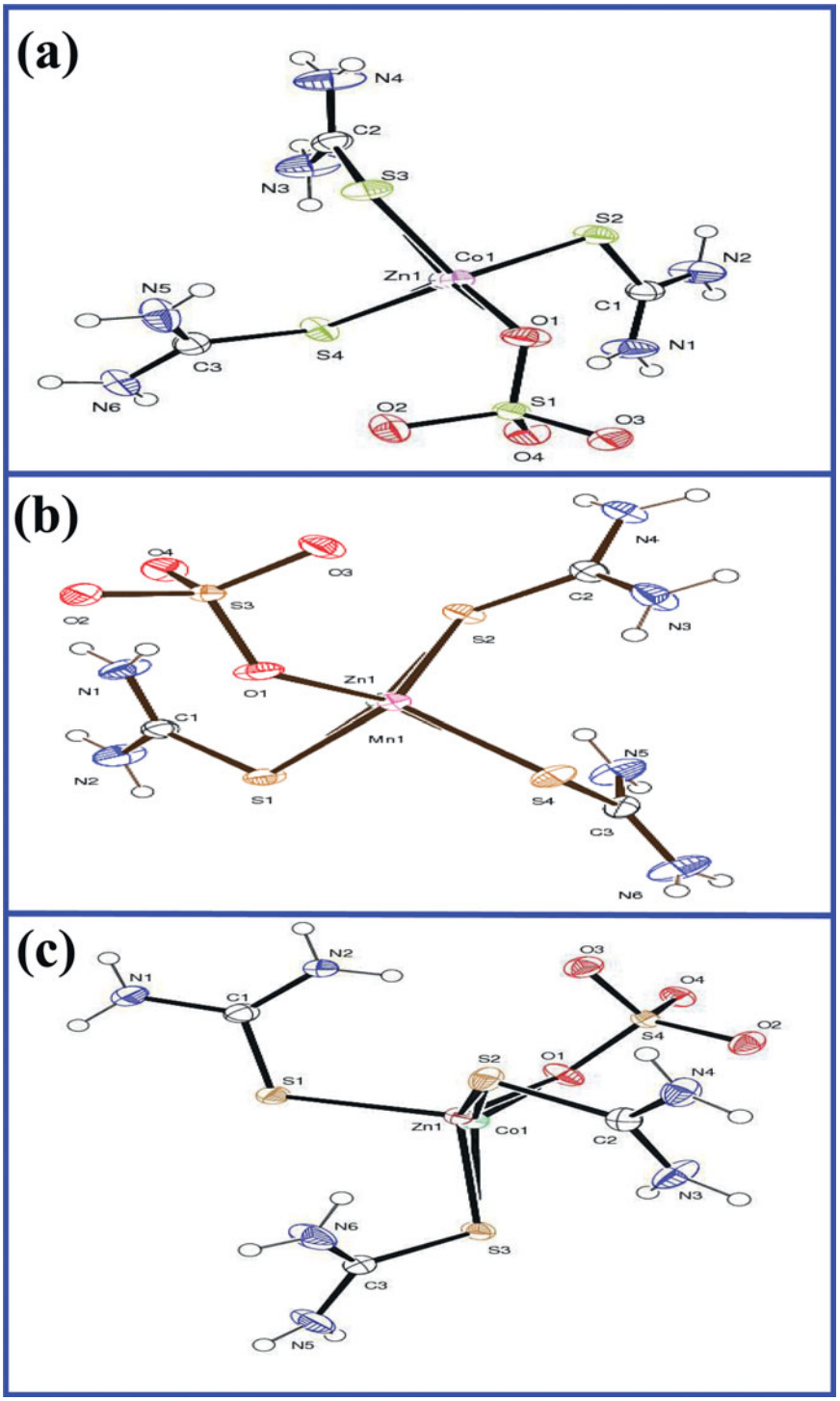

Figure 4. ORTEP diagram of (a) Co(II)-doped, (b) Co(II)+ Mn(II)-doped and (c) Co(II)+ Ni(II)-doped Crystals.

Table 2. Crystal data and structure refinement of co-doped ZTS

	Co(II)-doped	Co(II)- + Mn(II)-doped	Co(II)- + Ni(II)-doped
Molecular formula	$C_3H_{12}Co_{.12}N_6O_4S_4Zn_{.88}$	$C_3H_{12}Mn_{.08}N_6O_4S_4Zn_{.92}$	$C_3H_{12}Co_{.12}N_6O_4S_4Zn_{.88}$
Molecular weight	389.02	388.96	389.02
Unit cell parameters	$a = 11.158$ (3) Å	$a = 11.14240$ (10) Å	$a = 11.1719$ (2) Å
	$b = 7.7890$ (10) Å	$b = 7.7796$ (2) Å	$b = 7.8006$ (3) Å
	$c = 15.517$ (5) Å	$c = 15.5014$ (3) Å	$c = 15.5405$ (5) Å
	$\alpha = 90^\circ$	$\alpha = 90^\circ$	$\alpha = 90^\circ$
	$\beta = 90^\circ$	$\beta = 90^\circ$	$\beta = 90^\circ$
	$\gamma = 90^\circ$	$\gamma = 90^\circ$	$\gamma = 90^\circ$
Volume	1348.6 (6) Å^3	1343.71 (4) Å^3	1354.32 (7)Å^3
Crystal system	Orthorhombic	Orthorhombic	Orthorhombic
Space group	$Pca2_1$	$Pca2_1$	$Pca2_1$
Z	4	4	4
Wavelength (λ)	0.71073 Å	0.71073 Å	0.71073 Å
Temperature	293 (2) K	293 (2) K	293 (2) K
Calculated density	1.916 Mg/m^3	1.923 Mg/m^3	1.908 Mg/m^3
Absorption coefficient	2.389 mm^{-1}	2.396 mm^{-1}	2.379 mm^{-1}
$F(000)$	791	790	791
Crystal size	0.20 × 0.20 × 0.15 mm^3	0.35 × 0.30 × 0.25 mm^3	0.20 × 0.20 × 0.15 mm^3
Theta range for data collection	2.61 to 24.99°	2.62 to 25.00°	2.61 to 26.00°
Limiting indices	$-13 \leq h \leq 13$, $-9 \leq k \leq 9$, $-18 \leq l \leq 18$	$-13 \leq h \leq 13$, $-9 \leq k \leq 9$, $-17 \leq l \leq 18$	$-13 \leq h \leq 13$, $-6 \leq k \leq 9$, $-19 \leq l \leq 16$
Reflections collected/unique	11054/2358 [R(int) = 0.0265]	11600/2271 [R(int) = 0.0261]	6611/2483 [R(int) = 0.0218]
Completeness to theta	100.0%	100.0%	100.0%

Absorption correction	Semi-empirical from equivalents	Semi-empirical from equivalents	Semi-empirical from equivalents
Max. and min. transmission	0.7423 and 0.6231	0.5963 and 0.4536	0.7365 and 0.6326
Refinement method	Full-matrix least-squares on F^2	Full-matrix least-squares on F^2	Full-matrix least-squares on F^2
Data/restraints/parameters	2358/1/216	2271/19/215	2483/19/215
Goodness-of-fit on F^2	1.068	1.068	1.039
Final R indices [$I > 2\text{sigma}(I)$]	$R_1 = 0.0132$, w$R_2 = 0.0335$	$R_1 = 0.0131$, w$R_2 = 0.0321$	$R_1 = 0.0167$, w$R_2 = 0.0393$
R indices (all data)	$R_1 = 0.0137$, w$R_2 = 0.0337$	$R_1 = 0.0135$, w$R_2 = 0.0323$	$R_1 = 0.0178$, w$R_2 = 0.0396$
Absolute structure parameter	−0.002(6)	0.000(6)	0.010(7)
Extinction coefficient	0.0206(5)	0.0283(5)	0.0103(5)
Largest diff. peak and hole	0.162 and −0.154 e.Å^{-3}	0.146 and −0.160 e.Å^{-3}	0.222 and −0.198 e.Å^{-3}

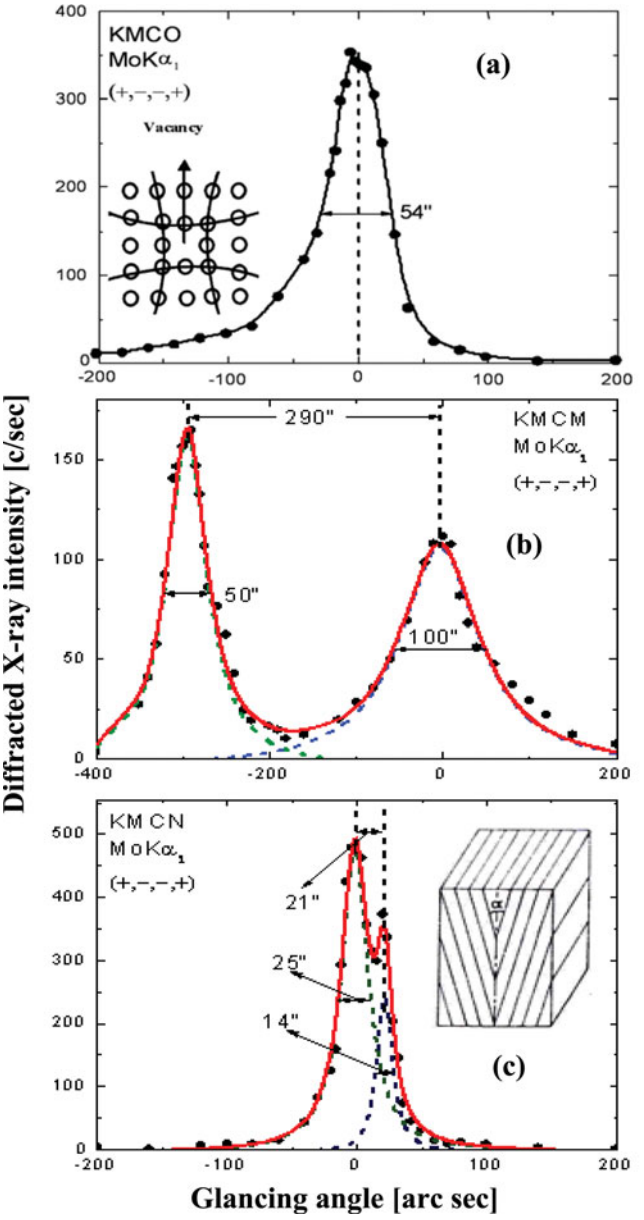

Figure 5. HRXRD curves recorded for (a) Co(II)-doped, (b) Co(II)+ Mn(II)-doped and (c) Co(II)+ Ni(II)-doped Crystals.

3.3. HRXRD

Figure 5 shows the high-resolution diffraction curves recorded for the doped single-crystal specimens using (123) diffracting planes in symmetrical Bragg geometry by employing the multicrystal X-ray diffractometer with Mo Kα_1 radiation. As seen in Fig. 5a, the DC contains a single peak indicating that the specimen is free from structural grain boundaries. The full width at half maximum (FWHM) of this curve is 54 arc sec which is somewhat

higher than that expected from the plane wave theory of dynamical X-ray diffraction [12] and reveals the presence of point defects and their aggregates. It is interesting to see the shape of the DC. The DC is asymmetric with respect to the Bragg peak position. For a particular angular deviation ($\Delta\theta$) of glancing angle (θ) with respect to the Bragg peak position (taken as zero for the sake of convenience), the scattered intensity is much more in the negative direction in comparison to that of the positive direction. This feature clearly indicates that the crystal contains predominantly vacancy type of defects than that of interstitial defects. This can be well understood by the fact that due to vacancy defects, the lattice around these defects undergo tensile stress [13] and the lattice parameter d (interplanar spacing) increases and leads to give more scattered (also known as diffuse X-ray scattering) intensity at slightly lower Bragg angles (θ_B) as d and sin θ_B are inversely proportional to each other in the Bragg equation ($2d \sin \theta_B = n\lambda$; n and λ being the order of reflection and wavelength, respectively, which are fixed). The inset in Fig. 5 shows the schematic to illustrate how the lattice around the defect core undergoes tensile stress. It may be mentioned here that the variation in lattice parameter is confined very close to the defect core which gives only the scattered intensity close to the Bragg peak. Long range order could not be expected and hence change in the lattice parameter is also not expected [14]. It may be worth to mention here that the point defects are more or less statistically distributed in the crystal. If the defects are not statistically distributed but distributed here and there as macroscopic clusters, then the strain generated by such clusters is larger leading to cracks and structural grain boundaries which can be seen very clearly in HRXRD curves with additional peak(s) as observed in our recent study on urea-doped crystals in ZTS at various levels of doping [11]. However, in the present experiments the diffraction curve does not contain any additional peak and indicates the absence of clustering of defects at macroscopic level. The single diffraction peak with reasonably low FWHM indicates that the crystalline perfection is fairly good.

On deconvolution of the diffraction curves (Fig. 5c), it is clear that the curve contains additional peaks which are away from the higher intensity peak. The additional peak corresponds to an internal structural very low angle boundary. For a better understanding, the schematic of a structural grain boundary is given as inset in Fig. 5c. As seen in the inset two regions of the crystal are misoriented by a finite angle α also known as tilt angle. Tilt angle may be defined as the misorientation angle between the two crystalline regions on both sides of the structural grain boundary. The two regions may be perfect. If the value of α is ≤ 1 arc min, we may call it as very low angle boundary. If $\alpha > 1$ arc min but less than a deg, we call it as low angle boundary. For more details of such structural grain boundaries including their affect on physical properties, reference is made available elsewhere [15,11]. The angular separation between the two peaks gives the tilt angle α which is 21 arc sec for the specimen crystal as seen in the Fig. 5c. The FWHM of the main peak and the low angle boundary are, respectively, 25 and 14 arc s. These relatively lower values reveal the fact that both the regions of the crystal are nearly perfect. These types of structural defects are probably generated in the crystals due to mechanical/thermal fluctuations occurred during the growth process and/or also due to fast growth [16]. It may be mentioned here that such minute defects could be detected with well-resolved peaks in the diffraction curve only because of the high-resolution of the diffractometer, characterized by very low values of wavelength spread i.e. $\Delta\lambda/\lambda$ and horizontal divergence for the exploring or incident beam, which are, respectively, around 10^{-5} and much less than 3 arc s of the multicrystal X-ray diffractometer used in the present studies. The influence of such defects may not influence much on the NLO properties. However, a quantitative analysis of such unavoidable defects

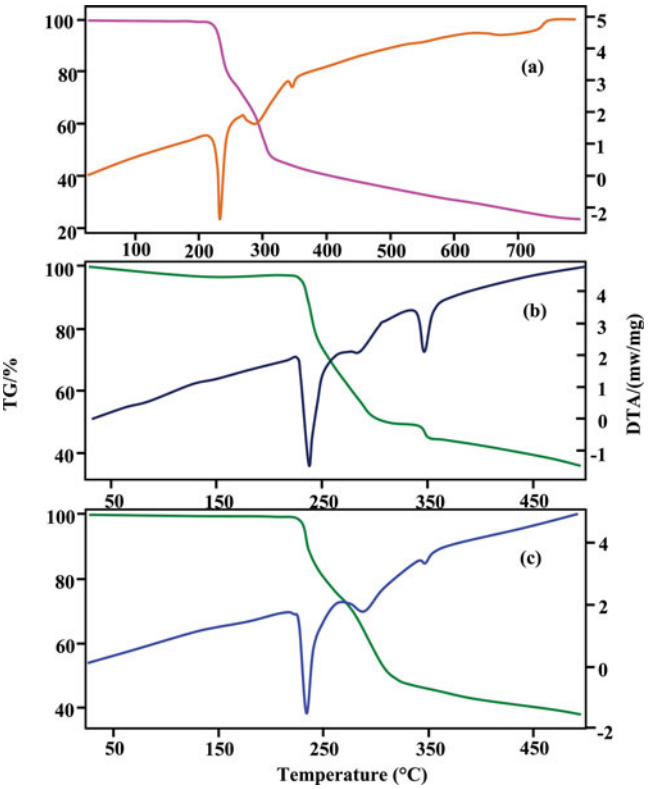

Figure 6. TG–DTA curves of (a) Co(II)-doped, (b) Co(II)+ Mn(II)-doped and (c) Co(II)+ Ni(II)-doped Crystals.

is of great importance, particularly in case of phase matching applications as explained in our recent article [17].

The nature of Fig. 5b is similar to that of Fig. 5c the additional peak corresponds to an internal structural low angle boundary with tilt angle 290 arc s. The FWHM of the main peak and low angle boundaries are 50 and 100 arc s, respectively. Though the specimen contains low angle boundaries, the relatively low angular spread (10 arc min) of the DC and the low FWHM values show that the crystalline perfection is reasonably good.

3.4. Thermal Studies

The simultaneous TG-DTA curves recorded in nitrogen ambient for all doped specimens are shown in Fig. 6. The absence of water of hydration in the molecular structure is indicated by the absence of weight loss around 100°C. No decomposition up to the melting point ensures the suitability of the material for application in lasers where the crystals are required to withstand high temperatures. The thermal stability of doped specimens is slightly enhanced by doping.

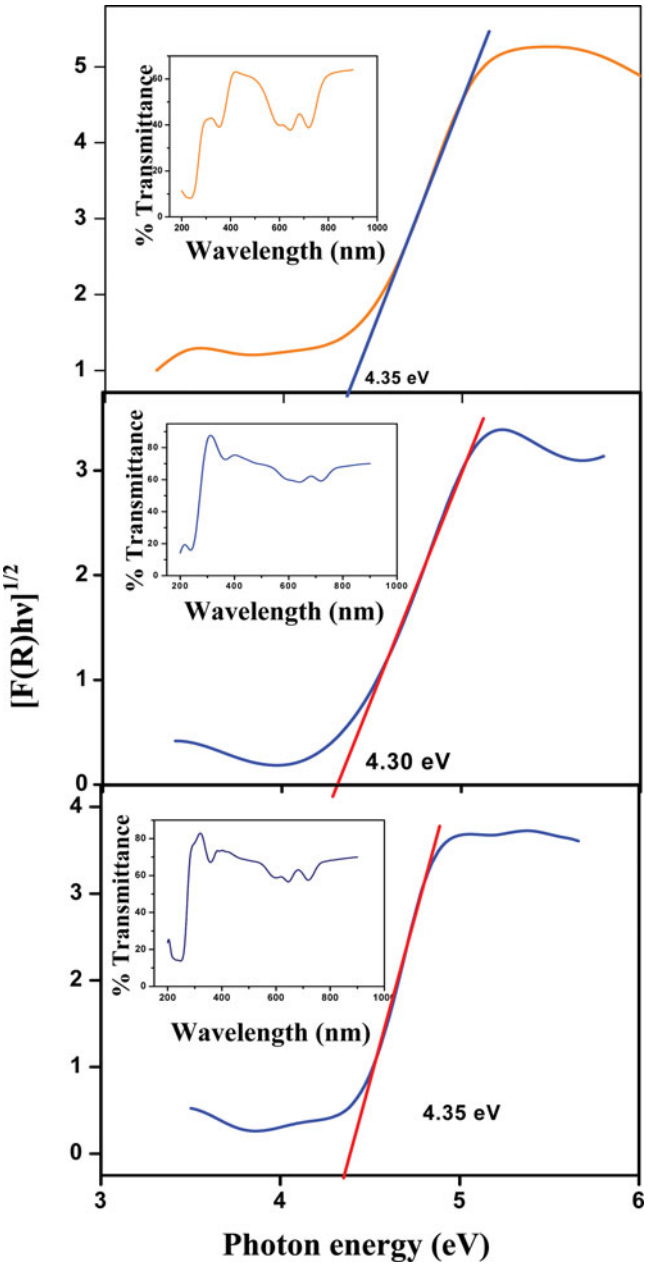

Figure 7. Tauc plots of (%Transmittance vs wavelength plot is given as inset) (a) Co(II)-doped, (b) Co(II)+ Mn(II)-doped and (c) Co(II)+ Ni(II)-doped Crystals.

3.5. Optical Transmission Studies

The UV-visible spectrum was recorded for all doped specimens. It is observed that doping alters the optical transmission. The band-gap energy of all the doped specimens were estimated from the Tauc plot, $[F(R)\ h\nu]^{1/2}$ vs $h\nu$ (eV) where $h\nu$ is the photon energy and

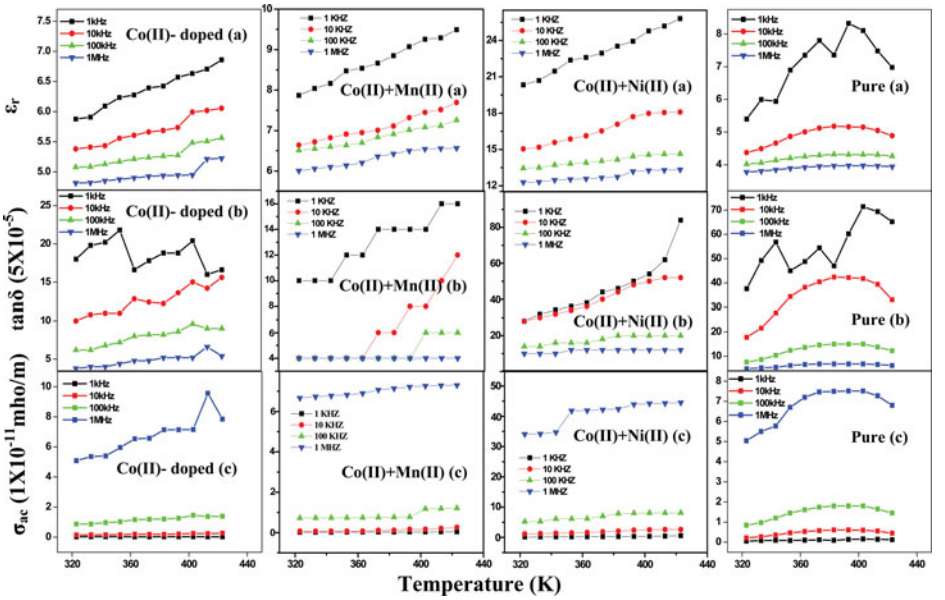

Figure 8. Dielectric measurements for (a) Co(II)-doped, (b) Co(II)+ Mn(II)-doped, (c) Co(II)+ Ni(II)-doped and (d) Pure ZTS Crystals.

F(R), the reflectance data obtained by Kubelka–Munk (theory provides correlation between reflectance and concentration) algorithm [18]. All band gap energies are fall in a close range (Fig. 7).

3.6. Dielectric Properties

The dielectric parameters, viz. dielectric constant, dielectric loss and AC conductivity increase with the increase in temperature (Fig. 8(a–d)). The ε_r and tan δ values decrease with increase in frequency while σ_{ac} increases with increase in frequency. Same type of behavior is exhibited by all doped specimens. The large value of dielectric constant at low frequencies may be due to contribution of all these polarizations. The decreased dielectric constant at higher frequencies could be due to the reduction in the space charge polarization. Space charge polarization is generally active at lower frequencies and high temperatures indicating the purity and perfection of the grown crystal. The increase in conductivity could be attributed to reduction in the space charge polarization at higher frequencies [19]. In the present study, dielectric constant varying proportionally with temperature is essentially due to the temperature variation of the polarizability [20]. The low ε_r value dielectric materials have potential applications in microelectronic industries.

3.7. SHG Efficiency

All doped specimens were subjected to SHG test. An Nd:YAG laser with a modulated radiation of wavelength 1064 nm was directed on the powder sample through a filter. The doubling of frequency was confirmed by the green radiation of wavelength 532 nm. Weak SHG signals particularly in Co(II)+Mn(II) and Co(II)+Ni(II) co-doping could be due to

partial cancellation of charge transfer because of the presence of the other foreign metal ion.

4. Conclusions

A close observation of XRD and FT-IR of pure and all doped ZTS specimens reveal some minor compositional variations and it was confirmed by single-crystal X-ray diffraction analysis. The studies indicate that the crystal undergoes considerable lattice stress as a result of doping. Single-crystal XRD analysis confirms the selective doping into the crystalline matrix of ZTS. Crystalline perfection is good in the case of single metal ion doping while co-doping with Co(II)+Mn(II) and Co(II)+Ni(II) results in structural grain boundaries. A normal dielectric behavior is observed for doped specimens.

Acknowledgments

The authors thank SAIF, IIT Madras, Chennai for providing single crystal XRD facility and Dr. C.K. Mahadevan, Physics Research Centre, S.T. Hindu College, Nagercoil for the support in dielectric studies. The authors thank Department of Science and Technology (DST), New Delhi, for the financial support through research grant No: SR/S2/LOP-0025/2010 and M. Rajasekar is grateful to DST for a project Fellowship.

References

[1] Gupta, S. S., & Desai, C. F. (1999). *Cryst. Res. Technol.*, *34*, 1329–1332.
[2] Ramabadran, U. B., Zelmon, D. E., & Kennedy, G. C. (1992). *Appl. Phys. Lett.*, *60*, 2589–2591.
[3] Sastry, P. U. (1999). *Solid State Commun.*, *109*, 595–598.
[4] Venkataramanan, V., Dhanaraj, G., Wadhawan, V. K., Sherwood, J. N., & Bhat, H. L. (1995). *J. Cryst. Growth.*, *154*, 92–97.
[5] Long, X., Wang, G., & Han, T. P. J. (2003). *J. Cryst. Growth.*, *249*, 191–194.
[6] Ramajothi, J., & Dhanuskodi, S. (2003). *Cryst. Res. Technol.*, *38*, 986–991.
[7] Bhagavannarayana, G., Kushwaha, S. K., Parthiban, S., & Meenakshisundaram, S. (2009). *J. Cryst. Growth*, *311*, 960–965.
[8] Meenakshisundaram, S., Parthiban, S., Sarathi, N., Kalavathy, R., & Bhagavannarayana, G. (2006). *J. Cryst. Growth.*, *293*, 376–381.
[9] Kurtz, S. K., & Perry, J. J. (1968). *J. Appl. Phys.*, *39*, 3798–3813.
[10] Lal, K., & Bhagavannarayana, G. J. (1989). *Appl. Crystallogr.*, *22*, 209–215.
[11] Bhagavannarayana, G., & Kushwaha, S. K. (2010). *J. Appl. Crystallogr.*, *43*, 154–162.
[12] Batterman, B. W., & Cole, H. (1964). *Reviews of Modern Phys.*, *36*, 681–717.
[13] Bhagavannarayana, G., Parthiban, S., & Meenakshisundaram, S. (2008). *Cryst. Growth Des.*, *8*, 446–451.
[14] Bhagavannarayana, G., Kushwaha, S. K., Shakir, M., & Maurya, K. K. (2011). *J. Appl. Crystallogr.*, *44*, 122–128.
[15] Bhagavannarayana, G., Ananthamurthy, R. V., Budakoti, G. C., Kumar, B., & Bartwal, K. S. (2005). *J. Appl. Crystallogr.*, *38*, 768–771.
[16] Bhagavannarayana, G., Rajesh, P., & Ramasamy, P. (2010). *J. Appl. Crystallogr.*, *43*, 1372–1376.
[17] Bhagavannarayana, G., Riscob, B., & Shakir, M. (2011). *Mater. Chem. Phys.*, *126*, 20–23.
[18] Kubelka, P., & Munk, F. (1931). *Zeitschrift fur technische Physik*, *12*, 593–601.
[19] Jonscher, A. K. (1997). *Nature*, *267*, 673–679.
[20] Priya, M., & Mahadevan, C. K. (2008). *Physica B*, *403*, 67–74.